Biogenic and synthetic MnO_2 nanoparticles: size and growth probed with absorption and Raman spectroscopies and dynamic light scattering

Alexandra V. Soldatova,[†] Gurusamy Balakrishnan,[†,^] Oyeyemi F. Oyerinde,[†,#] Christine A. Romano,[§,⊥] Bradley M. Tebo,[§] and Thomas G. Spiro*[,†]

[†]Department of Chemistry, University of Washington, Box 351700, Seattle, Washington 98195, United States

[§]Division of Environmental and Biomolecular Systems, Oregon Health & Science University, Portland, Oregon 97239, United States

*Corresponding Author: spiro@chem.washington.edu

ABSTRACT

MnO_2 nanoparticles, similar to those found in soils and sediments, have been characterized via their UV-visible and Raman spectra, combined with dynamic light scattering and reactivity measurements. Synthetic colloids were prepared by thiosulphate reduction of permanganate, their sizes controlled with adsorbates acting as capping agents: bicarbonate, phosphate, and pyrophosphate. Biogenic colloids, products of the manganese oxidase, Mnx, were similarly characterized. The bandgap energies of the colloids were found to increase with decreasing hydrodynamic diameter, D_h, and were proportional to $1/D_h^2$, as predicted from quantum confinement theory. The intensity ratio of the two prominent Mn–O stretching Raman bands also varied with particle size, consistent with the ratio of edge to bulk Mn atoms. Reactivity of the synthetic colloids toward reduction by Mn^{2+}, in the presence of pyrophosphate to trap the Mn^{3+} product, was proportional to the surface to volume ratio, but showed surprising complexity. There was also a remnant unreactive fraction, likely attributable to Mn(III)-induced surface passivation. The bandgap was similar for biogenic and synthetic colloids of similar size, but decreased when the enzyme solution contained pyrophosphate, which traps the intermediate Mn(III) and slows MnO_2 growth. The bandgap/size correlation was used to analyze the growth of the enzymatically produced MnO_2 oxides.

INTRODUCTION

Redox cycling of manganese is a key geochemical process in the environment.[1] Under aerobic conditions, Mn(IV) is the stable form and, in nature, occurs in a variety of Mn oxide minerals, which are typically composed of Mn(IV) with small amounts of Mn(III). Such Mn(III,IV) oxides are ubiquitous in soils and sediments.[2] In the absence of oxygen, anaerobic bacteria are capable of using MnO_2 as an electron sink to support their metabolism,[3-7] producing

24 aquo-Mn^{2+}, which is stable. Mn(II) can be oxidized to insoluble Mn(III,IV) oxides through both
25 abiotic and biotic processes in the environment. However, abiotic manganese oxidation is much
26 slower than biological oxidation, which is carried out by a variety of different bacteria and
27 fungi.[8-18] Some bacteria oxidize Mn(II) indirectly through the production of superoxide radical
28 (O_2^-), which oxidizes Mn(II) to Mn(III), subsequently forming MnO_2 by an as yet unknown
29 mechanism.[19-22] Other bacteria use peroxides to oxidize Mn(II) via calcium-binding animal heme
30 peroxidases (AHP),[23,24] but many others utilize O_2 directly via multicopper oxidases
31 (MCOs).[25,26] Microbial oxidation of Mn^{2+} is the likely origin of most MnO_2 in the environment.[14]
32 Consequently, the mechanisms of biogenic MnO_2 formation and maturation are of considerable
33 interest. Previous studies have involved whole organisms or fragments that support the reaction,
34 and interpretation has been uncertain because of the complexity of the molecular interactions in
35 these systems. Isolation of the responsible enzymes has proven difficult, although genomic
36 analyses implicate MCOs in a number of bacteria.[25-33] One of these, MnxG, has now been
37 expressed recombinantly, together with accessory proteins MnxE and MnxF as a multimeric
38 complex.[34,35] The mechanism of this enzyme has been shown to exploit the polynuclear
39 chemistry of manganese, in the oxidation states II, III, and IV, in order to overcome barriers to
40 electron transfer, and to nucleate MnO_2 nanoparticles.[36,37]

41 Biogenic MnO_2, similar to birnessite-like minerals—layered manganese oxides prevalent
42 in nature—is nanoparticulate (20−100 nm) and contains thin (3−5 nm) stacks of sheets composed
43 of edge-sharing MnO_6 octahedra, albeit with many Mn vacancies.[17,38-44] Upon ageing, these
44 particles undergo structural and redox transformation into more crystalline Mn oxides of various
45 mineral phases depending on conditions such as dissolved Mn(II) concentration, pH, temperature
46 and medium: a 10 Å phyllomanganate at low Mn(II) concentrations;[41] feitknechtite at high

Mn(II) concentrations;[41] triclinic birnessite in seawater (high Ca^{2+} concentrations);[42] and todorokite in uranium-rich solutions.[45] Other studies have observed evolution of the Mn oxide from poorly crystalline initial products to more crystalline phyllomanganate or triclinic birnessite.[20,46,47]

Their disordered structure, nanoscale morphology, and high surface area make biogenic MnO_2 nanoparticles particularly reactive toward sorption or oxidation of transition metals and other elements.[13,48] The high abundance of vacancies and structural defects contributes to their oxidative capacity,[49,50] giving them the ability to oxidize a variety of organic compounds, including humic substances.[51] Consequently, biogenic oxides are good candidates for clean water technologies for treating organic and inorganic pollutants. Additionally, there is interest in exploiting them as catalysts in photoelectrochemical water splitting[52-59] and in energy storage systems.[60-65] As with many metal oxides, the properties and potential applications of MnO_2, including bacterial MnO_2—from water oxidation to toxic metal sequestration—are influenced strongly by the particle size, which, in turn, determines the surface area and the density of highly reactive surface and edge sites.[66-70]

In this study, we use UV-visible (UV-vis) absorption spectroscopy, dynamic light scattering (DLS), Raman spectroscopy, and reduction kinetics to characterize synthetic MnO_2 preparations of varying particle size, and compare them with the Mnx-produced MnO_2 nanoparticles. The established database of spectroscopic information from the synthetic analogs can be used to evaluate the mechanism of biogenic manganese oxide growth and predict their potential environmental impact.

METHODS

MnO_2 synthesis. All chemicals were purchased from Sigma-Aldrich and were used without further purification. Solutions were prepared using Milli-Q deionized water. Manganese(II,III) oxide (Mn_3O_4) and manganese(III) oxide (Mn_2O_3) were purchased from Sigma-Aldrich. Solid phase birnessite was synthesized following the McKenzie method, by reduction of boiling $KMnO_4$ with 2 mole equivalent of concentrated HCl.[71] MnO_2 colloids were synthesized by the stoichiometric reduction of $KMnO_4$ with sodium thiosulfate ($Na_2S_2O_3$), following the method of Perez-Benito.[72,73] 0.5 mL of 0.1 M $KMnO_4$ was added to ~40 mL of water. Under gentle stirring, 0.5 mL of 39 mM $Na_2S_2O_3$ solution was added dropwise. The reaction proceeded according to the stoichiometry:[72]

$$8MnO_4^- + 3S_2O_3^{2-} + 2H^+ \rightarrow 8MnO_2 + 6SO_4^{2-} + H_2O.$$

Color change from purple to deep dark-brown was observed, indicating the formation of colloidal MnO_2. Water was added to dilute the solution to 50 mL, giving a final Mn concentration of 1 mM. The capping agents sodium phosphate (Na_3PO_4), sodium bicarbonate ($NaHCO_3$), or sodium pyrophosphate ($Na_4P_2O_7$, abbreviated thereafter as PP) were added as 5 mM solutions. The pH values of the resulting samples were 6.8, 7.4 and 7.2, respectively, and was 6.5 in the absence of capping agents. The brown transparent MnO_2 stock solutions were stored in the dark and were found to be stable for several months; no coagulation and settling occurred. Two sets of colloids were synthesized at different times. Both sets were characterized by UV-vis and DLS. One set, denoted as (1), was used to record Raman data. The other set (2) was used for reactivity measurements. The Mn(III) content of the colloids was less than 2.5% of the total Mn, as estimated[69] by incubation in the dark with 25 mM PP, and measurement of the 254 nm absorbance, characteristic of Mn(III) pyrophosphate complexes ($\varepsilon = 6562\ M^{-1}cm^{-1}$).

92 For reactivity measurements, MnO_2 colloids were centrifuged at 8000 rpm for 5 min
93 using Amicon Ultra 0.5 mL centrifugal filters (MWCO=30 kDa), then washed with deionized
94 water, and centrifuged again, repeating these steps three times to remove reagents and capping
95 ligands left from the synthesis. These steps did not alter the colloidal nature of MnO_2
96 preparations, resulting in essentially the same UV-vis absorption spectra (compare the spectrum
97 of MnO_2 prepared without capping ligands in Figure 1A and Figure 5A). Biogenic MnO_2 was
98 prepared using the Mn oxidase complex, Mnx, from *Bacillus sp.* strain PL-12, expressed and
99 purified as described previously.[34,74] Mnx enzyme (50 nM Mnx in 10 mM HEPES buffer,
100 pH=7.8) catalyzed oxidation of 1 mM manganese(II) chloride tetrahydrate ($MnCl_2 \cdot 4H_2O$) in the
101 presence of 0.5 mM PP, added to stabilize the MnO_2 colloidal product from coagulation and
102 precipitation. To obtain stable colloids of bio-oxides at higher concentrations for Raman studies
103 without pyrophosphate, a higher concentration of Mnx enzyme (~20 μM) was required to
104 catalyze the oxidation reaction.
105 *Spectroscopic measurements.* UV-vis absorption spectra and reactivity assays (190–1000 nm
106 spectral range) were monitored with an Agilent (Santa Clara, CA, USA) 8453 UV-vis
107 spectrophotometer, using a thermostatable multicell configuration with automated kinetic scan
108 capability and 10 mm path length cuvettes. The samples were stirred continuously with a
109 Spinette magnetic stirrer (Starna Cells, Atascadero, CA, USA). For reactivity measurements, the
110 washed colloids were resuspended in 10 mM sodium phosphate buffer (NaPi), pH=7.8, to yield a
111 concentration of ~50 μM in a 1 mL assay. 400 μM PP was added, and the reaction was initiated
112 by addition of 50 μM manganese sulfate ($MnSO_4$), see *Supporting Information* (SI).
113 Raman spectra were obtained with excitation between 407–752 nm from an Ar^+ laser
114 (Stabilite 2017, Spectra-Physics) and a Kr^+ laser (2080-RS, Spectra-Physics). Scattered light was

collected and focused onto a triple spectrograph (Spex 1877) equipped with a liquid nitrogen-cooled CCD detector (model 7375-0001, Roper Scientific) operating at −110 °C. The laser power measured at the sample was 15 mW. With this power, no photodecomposition or phase transformation of the samples was observed. Spectral acquisition times were typically 10 min. Raman spectra of colloids were obtained via backscattering geometry at room temperature in spinning NMR tubes, while spectra of solid oxides were collected from pressed pellets mounted on a copper multiple sample holder. For normalization of solid samples, the 982 cm^{-1} band from an $MnSO_4$ pellet was used as an external standard. Spectra of the standard were collected by a horizontal translation of the sample holder to ensure experimental conditions were unchanged. Spectra were calibrated with dimethyl formamide, and vibrational bands were fit with a mixed Gaussian-Lorentzian line shape using the GRAMS/AI software (version 7.0) from Galactic Industries.

The hydrodynamic particle sizes of MnO_2 colloids were evaluated by DLS with a Zetasizer Nano Series instrument (Malvern Instruments, Westborough, MA, USA), equipped with a He-Ne laser (λ=633 nm) and operated at a scattering angle of 173°. Samples were examined after filtering 1 mM MnO_2 solutions through a 0.2 μm acetate filter into 1 cm disposable plastic cuvettes. Measurements were carried out at 22°C. A medium viscosity of 0.954 mPa·s and a medium refractive index of 1.330 were set. The real and imaginary parts of the refractive index for MnO_2 were set to 2.4[75] and 0.01[76], respectively. Details of the DLS experiment to measure growth of enzymatically produced MnO_2 are given in the *SI*.

136 **RESULTS AND DISCUSSION**

137 **1. Synthetic MnO_2 Nanoparticles: Size–Band Gap Energy Correlation.**

138 Stable MnO_2 colloids were prepared by reducing 1 mM $KMnO_4$ with $Na_2S_2O_3$.[72,73] Consistent
139 with previous reports,[77-80] the MnO_2 colloids have broad UV-vis absorption bands between 250
140 and 700 nm, and a subsidiary peak at 210 nm (Figure 1A). The bands arise from ligand-to-metal
141 charge transfer (LMCT) transitions, with some Mn-3d→Mn-3d character: Density Functional
142 Theory (DFT) calculations on MnO_2[81,82] identified spin-dependent mixing between Mn-3d and
143 O-2p states, though the valence band has a dominant O-2p contribution, while Mn-3d states are
144 dominant in the conduction band.

145 ***1.1. Preparation of MnO_2 of different sizes.*** The main absorption band of MnO_2 shifts to higher
146 energy when anionic adsorbents are present during colloid preparation (Figure 1A, and Figures
147 S1 and S2A). MnO_2 has an isoelectric pH of 2.8,[83,84] so its surface charge is negative at near
148 neutral pH. While the oxyanions are also negatively charged, they are capable of adsorbing via
149 H-bonding to surface hydroxyl groups,[85] capping the particle surface and thereby limiting further
150 growth of the nanoparticles.[86] The magnitude of the energy shift is in the order
151 bicarbonate<phosphate<pyrophosphate. This is the order of expected adsorption strength:
152 bicarbonate is a weaker base than phosphate, which is in turn weaker than pyrophosphate. The
153 extent of shift also increases with increasing adsorbent concentration, consistent with a previous
154 observation of MnO_2 synthesis in the presence of phosphate.[86] As the shift increases, the
155 absorptivity decreases; its value in the absence of capping agents is 10^4 $M^{-1}cm^{-1}$ (Table S1 and
156 Figure S3). These spectroscopic changes are as expected from the quantum confinement effect in
157 nanoparticles,[87-92] and have been noted before for various MnO_2 preparations,[77,86,93-95] though
158 without any systematic quantification. In our MnO_2 set, particle sizes, estimated by DLS as

volume profiles of hydrodynamic diameters (Figures 1B and S2B), reveal that the diameters increase with increasing wavelength of the absorption bands (Table S1), consistent with quantum confinement as the determinant of the electronic energy. Because the oxyanion capping agents interact indirectly with MnO_2, via H-bonds,[85] they are unlikely themselves to perturb the electronic energies, and indeed the quantum confinement model adequately describes the size dependence of the spectra (section 1.3).

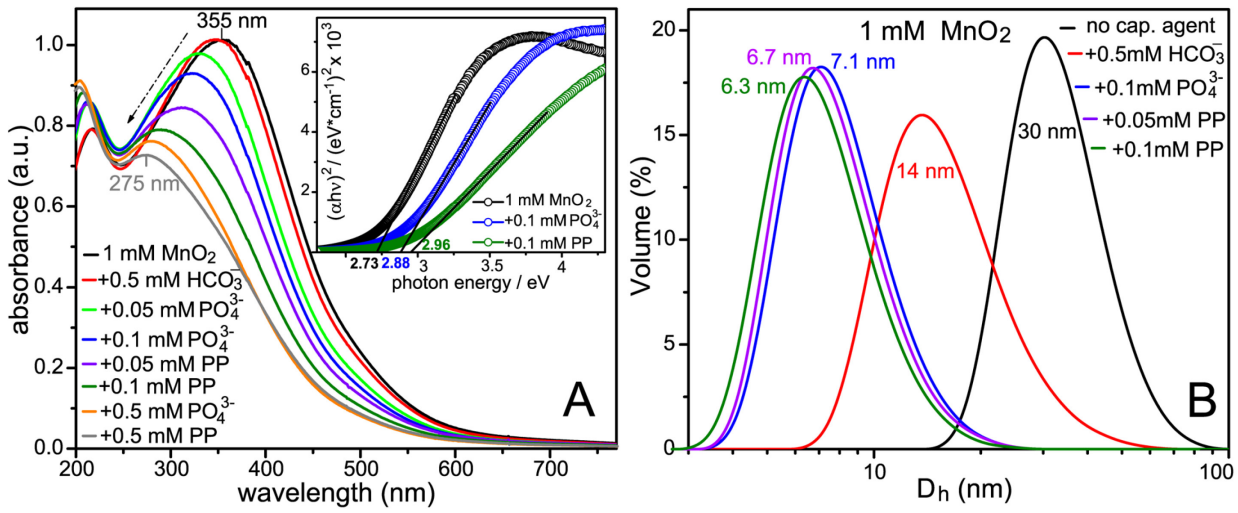

Figure 1. (A) UV-vis absorption spectra of 1 mM colloidal MnO_2 in water, prepared by reduction of $KMnO_4$ with $Na_2S_2O_3$ at room temperature, with indicated amounts of capping agents: bicarbonate, phosphate, pyrophosphate, or no additive (black line). *Inset*: Estimation of direct band gap energies from Tauc plot analysis for selected colloidal preparations. (B) DLS-measured hydrodynamic diameter of MnO_2 colloids.

1.2. Estimation of MnO_2 band gap energies. The UV-vis absorption spectra were used to estimate optical band gaps, E_g, using Tauc's method,[96] in which the absorption coefficient, α, (obtained from $\alpha = 2.3A/d$, where A is the measured absorbance and d is the path length of the cuvette) is plotted as a function of photon energy, $h\nu$, according to:

$$\alpha h\nu \sim (h\nu - E_g)^n, \qquad (1)$$

where n is the transition coefficient, which takes values ½ or 2, for direct and indirect allowed transitions. Vacancy-free hexagonal birnessite would have an indirect bandgap (the minimum energy of the conduction band and the maximum energy of the valence band occurring at

179 different values of the electron wavevector).[81] However, defect sites—vacancies and edge sites,
180 which are numerous in all synthetic and natural birnessites investigated experimentally to date—
181 distort the lattice and introduce a direct band gap, leading to more efficient light absorption.[81,97]
182 Colloids are rich in defects, and the large molar absorptivity (~10^4) is consistent with a direct
183 bandgap. We therefore used n=½ in the Tauc plots. The graph $(\alpha h\nu)^2$ *versus* the photon energy
184 has a linear region, which can be extrapolated to the abscissa to yield the bandgap energy (Figure
185 1A, *inset*). (The deviation from linearity at energies below the band gap, termed the "Urbach
186 Tail", is due to localized states from material defects.[98]) The energies obtained this way are
187 collected in Table S1. We also explored simpler ways to derive band gap energies from the UV-
188 vis absorption spectra (Figure S4), and found that the energy at which the absorbance is half the
189 maximum absorbance (λ_{half}) corresponds closely to the Tauc-derived band gap energy (Table S2
190 and Figure S5).

191 ***1.3. Quantum confinement in MnO_2 particles.*** When examined quantitatively, the band-gap
192 energies were found to increase linearly with $1/D_h^2$, where D_h is the hydrodynamic diameter
193 from DLS (Figure 2A). The inverse square dependence is as predicted for quantum confinement
194 in nanoparticles and observed in many different systems,[88] including colloidal gold
195 nanoparticles,[99] CdS,[100] Cu_2O,[101] ZnO,[102] and α-FeOOH[103]. Quantum confinement describes the
196 optical band-gap size dependence of MnO_2 even though its light absorption is mainly due to
197 distortions of the sheet structure coming from vacancies and surface sites[81,97]. Following Brus,[104]

198 $$E_g = E_g^{bulk} + \frac{\hbar^2\pi^2}{2R^2}\left[\frac{1}{m_e^*} + \frac{1}{m_h^*}\right] - \frac{1.8e^2}{4\pi\varepsilon\varepsilon_0 R} \quad (2)$$

199 E_g is the band-gap energy of a nanoparticle with radius R, E_g^{bulk} is the band-gap energy of the
200 bulk semiconductor, m_e^* and m_h^* are the electron and hole effective masses, ε is the dielectric
201 constant of the semiconductor, and ε_0 is the vacuum permittivity. The + term represents the

quantum confinement energies for the electron-hole pair, while the – term represents the electron-hole Coulomb interaction, which, for small particles, is small relative to the quantum confinement term. From the intercept, E_g^{bulk} = 2.73 eV, in excellent agreement with the values reported for birnessite-type MnO_2 thin films.[105,106] The slope of the $1/D_h^2$ plot yields μ_{eff}~1.1m_o, (m_o is the free electron mass) for the reduced effective mass of the exciton in MnO_2. This value is comparable to those reported for other transition metal oxide semiconductors.[107,108] With the established linear correlation, the UV-vis absorption spectroscopy provides a convenient way to estimate the size of MnO_2 particles.

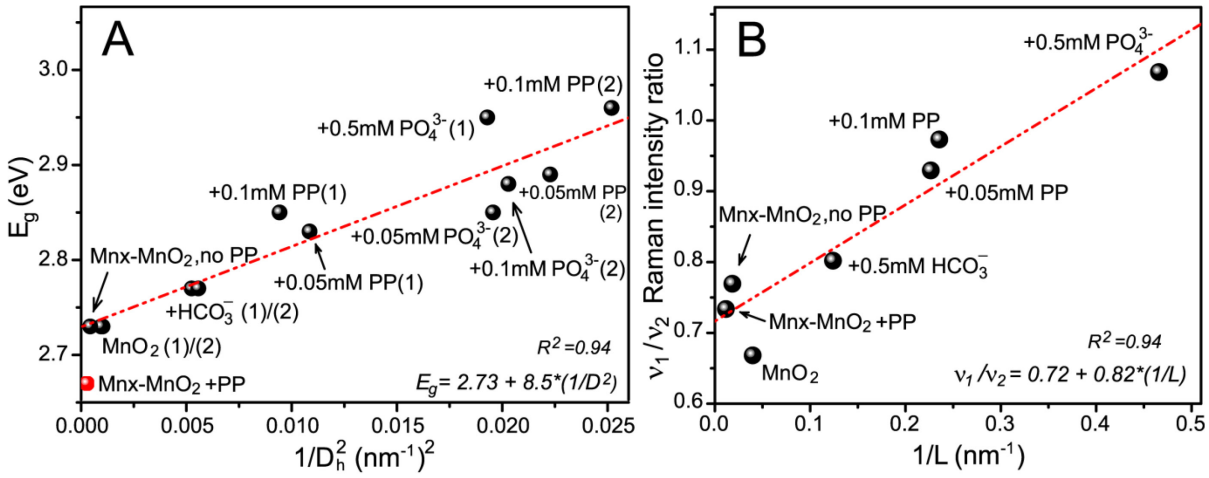

Figure 2. (A) Dependence of the band gap energy of MnO_2 colloids on nanoparticle size in the form of Brus equation (red line is a linear fit; the Mnx-MnO_2+PP point in red was excluded from the fit, *vide infra*).[109] (B) Dependence of the intensity ratios of Mn–O stretching Raman bands, ν_1 and ν_2, of colloids of different sizes (from subset (1) in Table S1) on nanoparticle sheet length (red line is a linear fit).

2. Synthetic MnO_2 Nanoparticles: Size-Dependent Raman Spectra.

We investigated Raman spectroscopy as a means of characterizing MnO_2 colloids (Figure S6). A number of Raman spectra have been reported for MnO_2, with somewhat inconsistent results. Solid MnO_2 is a black material that efficiently absorbs light and yields weak Raman signals. Turning up the laser power to overcome this difficulty can lead to photo-reduction to a variety of lower-valent Mn oxides, with different Raman spectra.[110-113] Using low laser power, we were

able to obtain powder spectra without photoproduct interference (Figure 3), which agree with previously published Raman spectra of layered birnessite-type materials.[114-116] Colloid solutions gave the same spectrum, albeit with altered relative intensities.

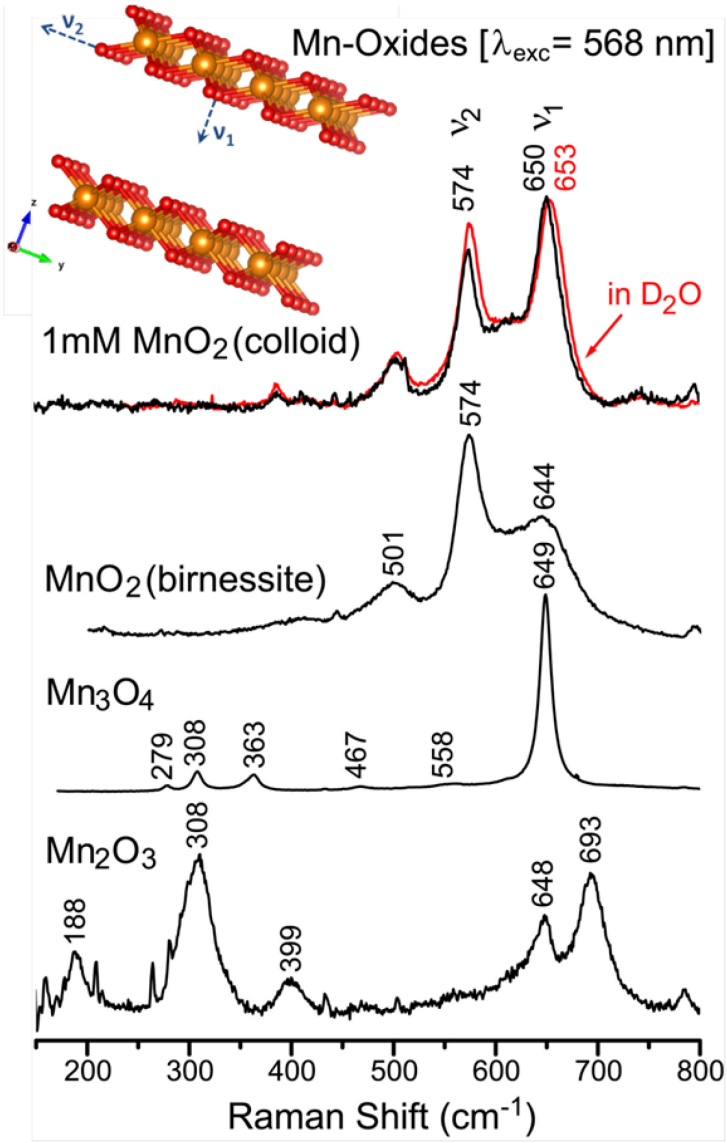

Figure 3. 568 nm-excited Raman spectra of solid-phase layered birnessite MnO_2, and Mn_3O_4 and Mn_2O_3 oxides, possible decomposition products of layered MnO_2 under the laser light. Top lines are Raman spectra of colloidal MnO_2 samples at 1 mM concentrations in H_2O (black) and D_2O (red). *Inset* shows two MnO_6 octahedral sheets, with ν_1 and ν_2 vibration stretching frequencies of layered-type hexagonal birnessite. The birnessite structure was visualized with VESTA 3,[117] using synthetic potassium birnessite crystal structure from Gaillot et al.[118]

Julien et al.[114] assigned the pair of strong bands at 575 and 650 cm^{-1} to Mn–O stretching vibrations within sheets of the MnO_6 octahedra (ν_2), and perpendicular to the sheets, along the

interlayer direction (ν_1) (Figure 3, *inset*); ν_1 can also be described as the totally symmetric stretch of the linked MnO_6 octahedra.[115] The frequency of the ν_1 band is sensitive to the interlayer distance, resulting from hydrated cation substitutions between the layers.[114,115] The position of the ν_2 band was also found to be sensitive to the size of interlayer cation, shifting to the opposite direction relative to the ν_1 band.[114,115] We observed a 3 cm^{-1} downshift of ν_1, while the ν_2 band remained unchanged, when the colloid was prepared in D_2O (Figure 3), an effect we attribute to H/D substitution at protonated O atoms bound terminally at sheet edges (see below).

When we recorded the spectra of MnO_2 colloids with different capping agents (Figure 4A), a systematic variation in the relative intensities of ν_1 and ν_2 became apparent. The ν_1/ν_2 intensity ratio increased for stronger capping agents, correlating with smaller particle size.

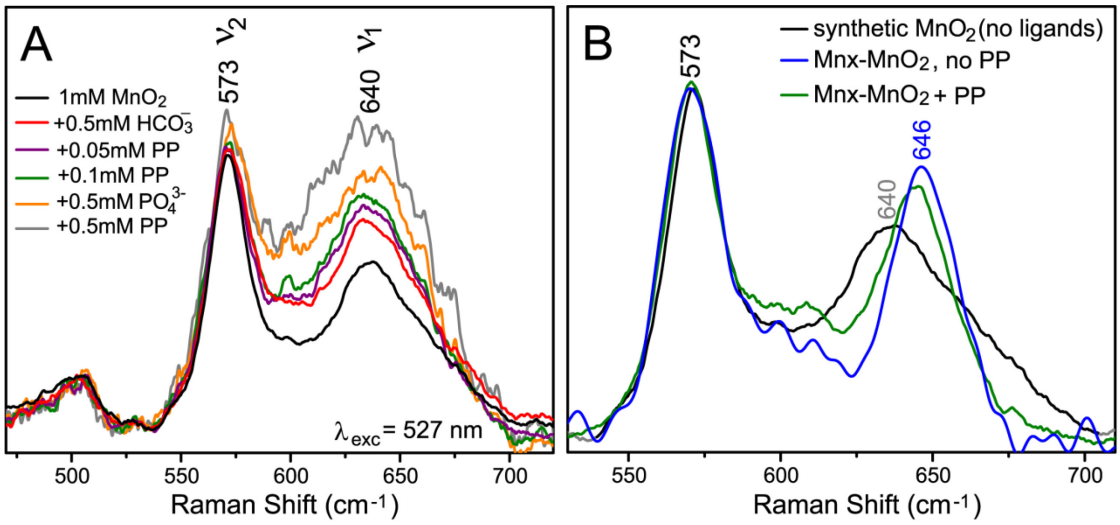

Figure 4. (A) Raman spectra of the synthetic MnO_2 colloids measured at 527 nm with 20 mW laser power at the sample and averaged for 20 min. The raw spectra were ν_2-normalized and smoothed (11 points). (B) ν_2-normalized Raman spectra of synthetic colloidal MnO_2 in water prepared without capping ligand (black line; the same as in (A)) and colloidal bio-MnO_2 produced by 50 nM Mnx in the assay without capping ligand (blue line) and in the presence of pyrophosphate (green line).

Since MnO_2 particles have sheet geometries,[119,120] the DLS-derived hydrodynamic diameter is approximated as the diameter of a hypothetical sphere represented by the nanosheets. Lotya et al.[121] demonstrated that the mean sheet length for such particles is given by:

$$L = (0.07 \pm 0.03) D_I^{(1.5 \pm 0.15)} \quad (3)$$

where D_I is the DLS-measured peak position of intensity size distribution (Table S1). Intriguingly, the ν_1/ν_2 intensity ratio correlates linearly with 1/L (Figure 2B). A particle size dependence is unexpected for assignment to vibrational modes intrinsic to the MnO_2 sheets.[114] Moreover, the D_2O/H_2O shift observed for the ν_1 band requires exchangeable protons, which occur on the terminal OH groups of edge sites. We propose that the Mn–OH stretching mode associated with edge sites happens to be coincident with the out-of-plane sheet mode, ν_1, whose apparent relative intensity therefore increases with decreasing particle size.

A 1/L dependence is expected for the particle edge-to-volume ratio. For a stack of *c* square sheets of length L, there are 4 edges per sheet, of total extent 4L*c*, while the volume is L^2c. The ratio is then 4/L. If "ν_1" is a composite band, the Raman intensity should be the sum of the superposed edge mode, ν_e, and the out-of-plane sheet mode, ν_1. The former should be proportional to the number of edge Mn atoms, *e*, while the latter, being intrinsic to the bulk of the particle, should be proportional to the total number of Mn atoms, *n*. For the in-plane sheet mode, ν_2, the intensity should also be proportional to *n*. The intensity ratio should then be:

$$I_1/I_2 = (j_1 n + j_e e)/j_2 n = j_1/j_2 + (j_e/j_2)(e/n) \; ; \qquad (e/n) = 4/L \qquad (4)$$

where the j_1, j_2, and j_e are molar scattering factors for ν_1, ν_2, and ν_e. The 1/L plot (Figure 2B) gives j_1/j_2 as the intercept (0.72), and $4j_e/j_2$ as the slope (0.82). If the sheets are indeed square, then $j_e/j_2 = 0.2$, a plausible value. All the modes involve Mn–O bond stretching and should have comparable polarizabilities, with allowance for some cancellation or reinforcement, depending on the eigenvectors of the modes. Thus, the Raman intensity ratio of the two prominent Mn–O stretching bands varies with particle size in a manner consistent with a superposition of internal sheet and edge site scattering. We note that a similar trend in the two main Raman band

intensities was observed as a function of size of a cation incorporated between the layers under low potential in thin-film MnO_2 electrodes in different electrolytes.[115]

3. Size-Dependent Reactivity of Synthetic MnO_2 Nanoparticles.

We assessed the size-dependent reactivity of the synthetic MnO_2 colloids with Mn(II), which reduces Mn(IV) to Mn(III).[41,73,122,123] In the presence of PP as a trapping agent for Mn(III),[124] the reaction can be monitored via the decrease in MnO_2 absorbance, and the concomitant rise of the 260 nm band due to Mn(III)PP (Figure 5A and Figure S7). Colloidal MnO_2 does not precipitate during the reaction: no visible precipitates and no significant absorbance increase above 700 nm from nanoparticle scattering could be seen.

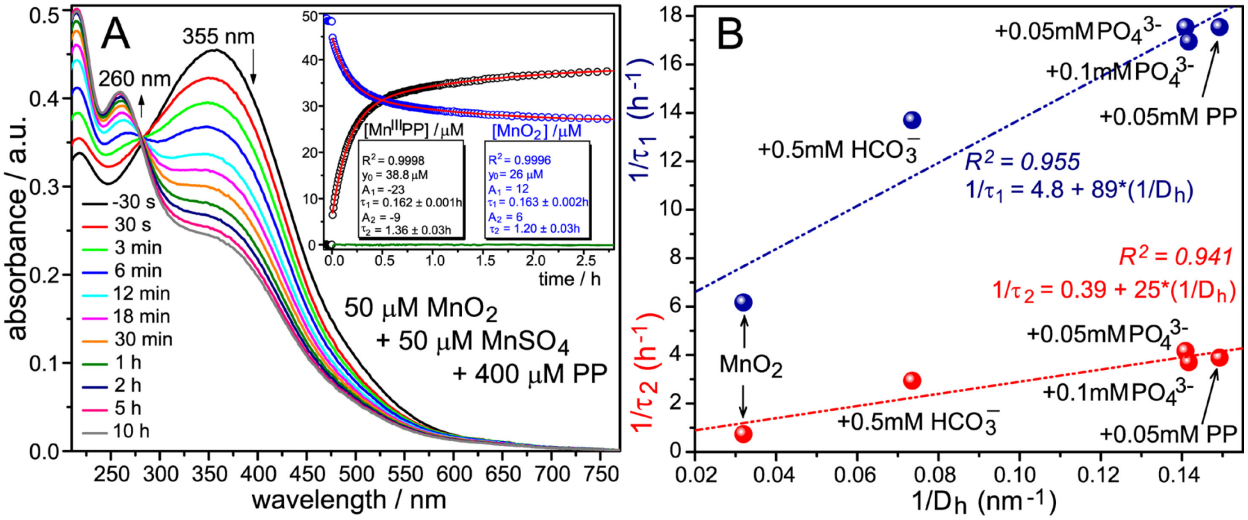

Figure 5. (A) Evolution of the UV-vis absorption spectra after addition of 50 μM $MnSO_4$ to ~50 μM synthetic MnO_2 colloids (λ_{max} = 355 nm) in 10 mM NaPi buffer, pH 7.8, in the presence of 400 μM PP, added to trap Mn(III) product (260 nm band). *Inset* shows concentration time profiles for Mn(III)PP (black points) and MnO_2 (blue points), obtained after absorption spectral data were converted to concentrations (see Method and *SI* for details), and fitted to a double-exponential function (red lines). The optimized parameters from the fit are indicated, together with the residual from the fit (green line). (B) $1/D_h$ dependence of τ_1 (blue points) and τ_2 (red points) obtained from fitting the MnO_2 reactivity data with a double-exponential function in Figure 5A and Figures S8 and expressed as rates.

The clear isosbestic point, maintained during the reaction, reveals a simple two-component mixture. Despite this evidence for a clean conversion of the reactants, Mn(II) and MnO_2, to the product, Mn(III)PP (Figure 5A), the kinetics are unexpectedly complex, with a fast phase, <30 s

297 (the mixing time), followed by two slower phases, ~0.1 h, ~0.5 h, and a substantial amount of
298 unreactive phase (~50% of the initial MnO_2). Adsorption of Mn(II) on MnO_2 is rapid at pH 5 (<1
299 sec),[125] and would be even faster at pH 7.8 because a proton is released in the process. (Although
300 the capping agents could in principle retard Mn(II) adsorption, displacement of these ionically
301 held oxyanions should be rapid, and, in any event, they were largely removed by washing and
302 centrifugation, prior to the reactivity measurements.) Thus, Mn(II) adsorption is not rate-limiting
303 on our time scale. After the initial phase, the time course of MnO_2 reduction, and of Mn(III)PP
304 growth, can be fit to two successive exponentials (Figure 5A, *inset*). However, even at 2.5 h,
305 about half of the MnO_2 remains unreacted, indicating a large refractory fraction. Reaction rates
306 were determined for the colloids prepared with capping agents (Figure S8), and also for different
307 concentrations of Mn(II) and of MnO_2 (Figure S9). The obtained rates show a clear correlation
308 with MnO_2 particle size (Figure 5B) for both of the measured phases, following a $1/D_h$
309 dependence. Thus, reactivity is dependent on the surface/volume ratio. Recent studies of metal
310 ion adsorption on birnessite have demonstrated the dominance of surface (edge) sites,[67,126-129]
311 and previous dissolution kinetics of manganese oxides indicated largely oxide surface
312 processes.[130] Nevertheless, the intercepts (rates for infinite size) are non-zero, suggesting that
313 interlayer sites also contribute to reactivity. No doubt the change in bandgap with particle size
314 also contributes to reactivity, since the Mn(IV) reduction potential should increase with
315 increasing band gap. This effect would contribute to the slope of the $1/D_h$ dependence.

316 The unreactive phase is likely due to some Mn(III) escaping the PP trapping agent and
317 remaining in the particles. It might migrate to vacancy sites and transform the lattice to a less
318 reactive structure, like the hexagonal-orthogonal transformation observed by Zhao et al.[131] for δ-
319 MnO_2 upon reaction with Mn(II). Lowered MnO_2 reactivity was also noted during continued

320 oxidation of fulvic acid as the accumulating Mn(III) entered interlayer and vacancy sites.[132]
321 Alternatively, the Mn(III) might form a surface precipitate of MnOOH or Mn_3O_4, inhibiting
322 further reaction, similar to the FeOOH and $MnFe_2O_4$ phases formed during reaction of MnO_2
323 with Fe(II) that also slows with time,[133] or to the Zn(II)-Mn(III) phases when Zn(II) sorption on
324 birnessite was investigated in the presence of Mn(II).[134] Likewise Wang et al.[128] observed a loss
325 in reactivity with time of δ-MnO_2 samples toward Co(II) oxidation, perhaps due to Co(III) and
326 Mn(III) oxides. MnO_2 surface passivation due to formed Mn(II)/Mn(III) phases was also invoked
327 to account for loss in MnO_2 reactivity during arsenic oxidation.[135,136] Surface passivation seems
328 the likelier explanation for our results, since the fraction of Mn(III) remaining in the particles
329 must be small, in view of the nearly stoichiometric ratio of Mn(III)PP accumulating in solution
330 to the MnO_2 consumed. Even though the detailed mechanism of the reaction and the nature of
331 the unreactive phase warrant further investigation (see *SI* for further elaboration on the
332 mechanism), the findings clearly demonstrate that while particle size determines reactivity, a
333 substantial fraction of the MnO_2 becomes unreactive as Mn(III) accumulates.

334 **4. Characterization of Enzymatically Produced MnO_2.** In the environment, manganese oxides
335 are thought to be primarily derived through microbial processes. These biogenic Mn oxides are
336 mainly nanocrystalline phyllomanganates with hexagonal sheet symmetry, similar to synthetic δ-
337 MnO_2 or hexagonal birnessite, with an Mn oxidation state between 3.7 and 4.0.[17,20,38-42,137] Thus,
338 the established correlation for synthetic MnO_2 particles might be used to characterize the
339 enzymatically produced MnO_2 particles.

340 ***4.1 Band gap energy and Raman spectra of Mnx-produced MnO_2.*** In our previous studies
341 during Mn(II) oxidation by the bacterial enzyme complex Mnx to form MnO_2 nanoparticles,[36]
342 we found that as the MnO_2 absorption band grows, it shifts steadily to longer wavelengths (red-

shift), consistent with increasing nanoparticle size as well as particle concentration. At the end of the enzymatic reaction, the MnO_2 band position was essentially the same as that of synthetic colloid prepared without a capping agent (Figure 6A).

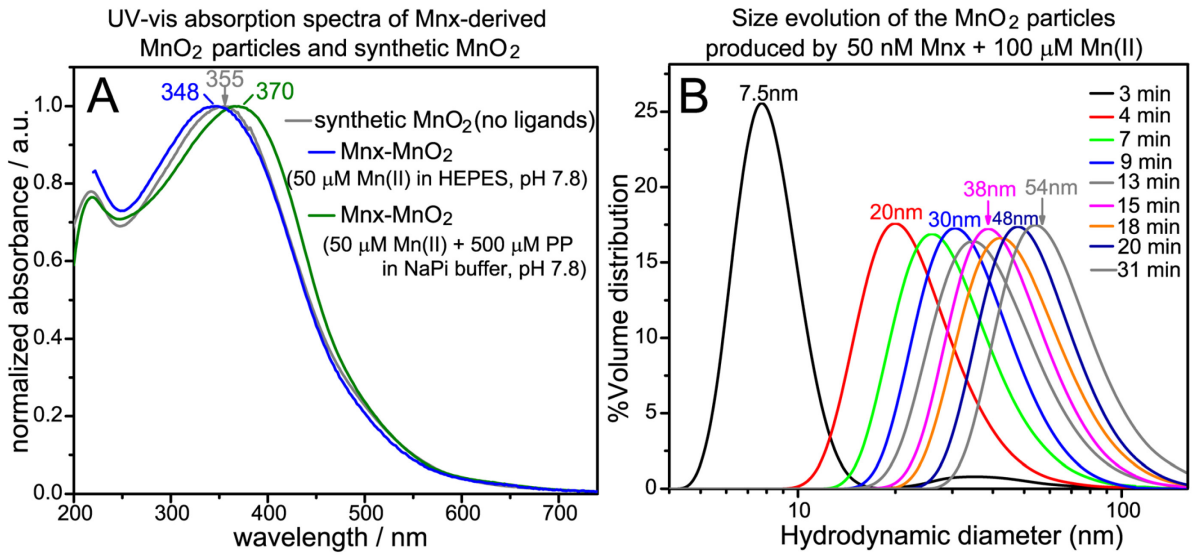

Figure 6. (A) Normalized UV-vis absorption spectra of synthetic colloidal MnO_2 in water prepared without capping ligand (gray line) and colloidal bio-MnO_2 produced by 50 nM Mnx in the assay without (blue line) and in the presence of pyrophosphate (green line). (B) Evolution of MnO_2 nanoparticle sizes formed during oxidation of 100 μM $MnSO_4$ catalyzed by 50 nM Mnx in HEPES buffer (pH=7.8) as measured by DLS at specified times.

DLS profiles, taken as a function of time during Mnx-catalyzed oxidation of Mn(II), capture the continuous growth of the MnO_2 particles (Figure 6B). This growth coincides with MnO_2 accumulation[36] (Figure 7), confirming that the nanoparticles increase in size as well as number as the reaction proceeds. At the end of the reaction, the Mnx-produced colloids had a 50% larger average diameter than the uncapped synthetic one (~54 nm *vs* 32 nm), despite having nearly the same band gap (Table S1 and Figure S11).

When pyrophosphate is present in the Mnx assay (to trap Mn(III) intermediate in the enzymatic studies[37]), the resulting MnO_2 has a red-shifted absorption maximum (370 nm, Figure 6A) and a still larger average diameter (~60 nm) with a broadened distribution—an effect that was also observed when birnessite-like material was obtained via photochemically assisted

362 superoxide oxidation of Mn(II) in the presence of increasing amount of PP.[95] The band-gap
363 energy is anomalously low for the biogenic MnO_2 when PP is present, falling off the quantum
364 confinement plot in Figure 2A. We speculate that the biogenic colloid has a higher defect density
365 than the synthetic colloids, the resulting sheet distortion lowering the excitation energy.

366 Raman spectra of Mnx-produced MnO_2 have bands similar to those of birnessite and
367 synthetic MnO_2, confirming earlier findings that Mnx produces birnessite-like layered MnO_2
368 minerals (Figure 4B). The ν_2 band due to Mn–O vibrations along the chains of the MnO_6
369 octahedra is the same as in the synthetic colloids. However, the biogenic colloids show narrowed
370 ν_1 peaks, which have higher wavenumber than the synthetic colloids (646 cm^{-1} *vs* 640 cm^{-1}).
371 Because the final particles are large, 50–60 nm, the 640 cm^{-1} edge mode, ν_e, is expected to be
372 relatively weak, and we infer that the out-of-plane sheet mode, ν_1, is shifted away from it,
373 narrowing as a result. Nevertheless, the ν_1/ν_2 intensity ratios fall on the size correlation
374 determined for the synthetic colloids (Figure 2B and Table S1).

375 ***4.2. Particle growth of Mnx-produced MnO_2.*** The evolution of the MnO_2 absorption band
376 during Mnx-catalyzed Mn(II) oxidation has been deconvoluted via multivariate analysis into
377 enzyme reaction and nanoparticle production time courses.[36] The latter showed a sigmoidal
378 increase in MnO_2 concentration, characteristic of nanoparticle nucleation followed by growth.
379 The present DLS measurements show that the average size of the particle grows linearly,
380 slowing down as the reaction nears completion (Figure 7). (Though a more complex growth
381 mechanism for these platy minerals is envisioned, its resolution by the time-resolved imaging
382 techniques being awaited). The linear increase in D_h is consistent with the sigmoidal increase in
383 MnO_2 concentration, if we consider that the volume of the particles is proportional to
384 concentration and also to the cube of the diameter. The sigmoidal growth curve in fact yields a

straight line over most of the time course when the cube root of the concentration is plotted against time (Figure S12).

The DLS measurements also yield a polydispersity index, PdI, a dimensionless measure of the breadth of the size distribution. The PdI values can range from 0 (monodisperse) to 1 (all sizes). Usually samples have PdI between 0.1 and 0.7. The PdI parameter of the Mnx-produced particle steadily decreased as the average size increased (Figure S12, *inset*), consistent with a nucleation/growth model (and inconsistent with Ostwald ripening,[138,139] which *increases* polydispersity with time[140-142]). Following Clark,[141] we plot log(PdI/PdI_0)-*versus*-R/R_0 (Figure 7, *inset*), where R_0 is the zero-time extrapolated value of $D_h/2$, 4.3 nm, and PdI_0 ~0.425 is the zero-time polydispersity index. The plot approaches the optimal limit for size focusing ($PdI/PdI_0 \rightarrow 1/8$ at $R/R_0 \rightarrow 8$), indicating that the growth of Mnx-produced MnO_2 is controlled by the continuous enzymatic supply of pre-nucleus particles on the time scale of nanoparticle growth, leading to narrowing of the size distribution.

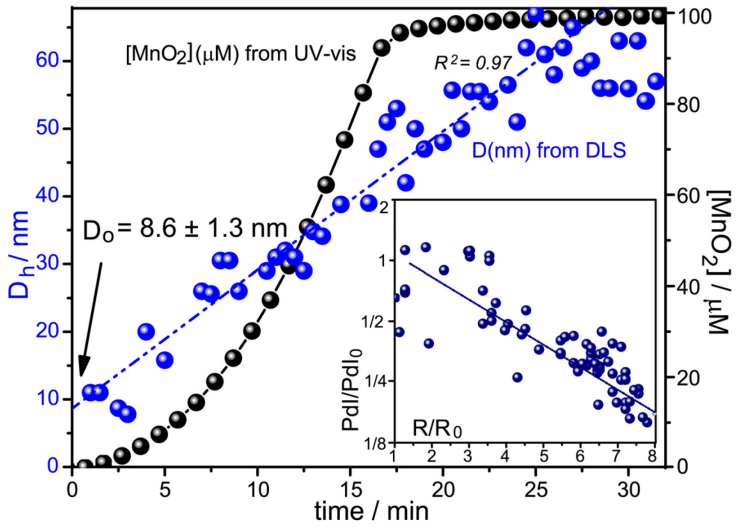

Figure 7. Time course of MnO_2 concentration increase (black points) from the UV-vis experiment obtained during oxidation of 100 μM $MnSO_4$ catalyzed by 50 nM Mnx in HEPES buffer (pH=7.8), with the superimposed time evolution of the hydrodynamic diameter of the MnO_2 particles (blue points) from the DLS measurements. The blue dotted line is a linear fit of the nanoparticle diameter increase, which could be extrapolated to time zero to give the diameter of nucleus of 8.6 nm. *Inset*: MnO_2 size-focusing plot obtained during Mnx-catalyzed oxidation of Mn(II), as measured by DLS. $R=D_h/2$ and R_0

405 corresponds to the zero-time radius (4.3 nm) of the particles, and PdI is the polydispersity index, whose
406 zero time value (PdI_0) was estimated to be 0.425 (see Figure S12, *inset*).

407 The early product of the enzyme reaction[36] has an absorption maximum at ~280 nm, suggestive
408 of a 7.5±0.7 nm nanoparticle (see Figure S11). This is close to the extrapolated D_h at zero time
409 (8.6 nm, Figure 7) and is likely the size of the nucleus from which the nanoparticle then grows.
410 The enzyme mechanism, inferred from kinetic analysis, suggests a dinuclear $[Mn(IV)O]_2$
411 complex as the initial product of Mn(II) oxidation.[37] A large number of these would be required
412 to assemble the nucleus (the number is hard to estimate because of uncertainty in the size of the
413 hydration layer, which can extend up to 5 nm for metal oxides[143]). Subsequently, growth would
414 occur by accretion of the product complexes, likely via oriented attachment.[144-147]

415 **5. Environmental Implications.** Characterizing the nanoparticulate nature of MnO_2 deposits or
416 preparations is of fundamental importance to predicting their reactivity. This work demonstrates
417 direct correlations among MnO_2 particle size, edge site populations, and reactivity, which are
418 conveniently monitored by UV-vis absorption and Raman spectroscopies and DLS.

419 The reactivity time course is complex for MnO_2 nanoparticles, and a substantial fraction
420 can remain unreacted, likely due to surface passivation by accumulating Mn(III). This
421 phenomenon is a constraint on evaluating the role of MnO_2 in environmental oxidation and
422 sequestration processes. For example, arsenic in ground water is a serious health problem of
423 global proportions,[148,149] and there is great interest in the potential of MnO_2 to remediate arsenic
424 *in situ*, or in drinking water filters.[150-152] Arsenate (As^V) is strongly adsorbed on MnO_2, as well as
425 Fe oxides surfaces, and arsenite (As^{III}) can be oxidized by MnO_2.[151,153-155] This is important as
426 As^{III} is the more toxic form of arsenic, and is also more mobile.[156,157] Thus, MnO_2 oxidation of
427 As^{III} to the strongly adsorbed As^V is an important determinant of groundwater arsenic

428 contamination, and of remediation strategies. Surface passivation limits the oxidation
429 capacity,[135,136,158] and further mechanistic studies may open routes to circumventing passivation.

430 Biogenic MnO_2 nanoparticles are of particular interest because their smaller size and high
431 density of reactive sites increase their reactivity toward organic substrates and metal
432 sequestration. This work elucidates the formation of MnO_2 nanoparticles from the Mnx MCO
433 complex. This enzyme is produced by several Mn-oxidizing *Bacillus* sp., and is found in the
434 exosporium—a complex structure of carbohydrates and proteins that surrounds the spore coats of
435 some bacterial spores. No doubt these organic molecules interact with the bio-MnO_2
436 nanoparticles, *en route* to the particles' deposition around the spores. For example, an early X-
437 ray study of Mn(II) oxidation by exosporium[159] found evidence for locally abundant Mn(III)
438 within the spore clumps, probably formed as a result of spore-mediated chelation of Mn(III)
439 intermediates. Abundance of organic Mn(III) chelators in the exosporium may also trigger
440 radical reactions with ultimate production of peroxide species, capable of additional oxidation of
441 Mn(II) to form MnO_2, thereby modifying the pure enzymatic MnO_2 product. Moreover, cell
442 surfaces can template emerging MnO_2, resulting in uni-directional nanoparticle growth. To
443 delineate these processes and evaluate modifications of the nanoparticles produced by whole
444 bacterial cells, an unobstructed view of enzymatic MnO_2 production, in the absence of additional
445 organic matter, is needed. Since MCOs are implicated in phylogenetically diverse groups of Mn-
446 oxidizing bacteria, studies with the purified Mnx protein provide a foundation for understanding
447 manganese mineralization across the microbial world.

448 The Mnx product itself may provide guidance toward improving the preparation of MnO_2
449 nanoparticles for potential uses. For example, our finding indicates that the nanoparticulate
450 nature of biogenic MnO_2 results from efficient enzymatic Mn(II) oxidation, which exceeds the

Ostwald ripening rate, leading to a narrow nanoparticle distribution. It is thus possible to influence the MnO_2 enzymatic production rate to control the final MnO_2 particle size distribution and optimize reactivity for technological applications.

ASSOCIATED CONTENT

Supporting Information: The Supporting Information is available free of charge on the ACS Publications website.

UV-vis absorption and DLS data for two sets of synthetic MnO_2 colloids; dependence of extinction coefficient of the MnO_2 colloids on the band gap energy; alternative ways to estimate band gap energies from the UV-vis spectra; characterization of solid-phase birnessite by UV-vis and Raman spectroscopies; additional results of the reactivity measurements; UV-vis absorption spectra of early and aged MnO_2 products from the Mnx-catalyzed Mn(II) oxidation reaction; time evolution of the Mnx-catalyzed MnO_2 formation as measured by UV-vis and DLS.

AUTHOR INFORMATION

[^]Present Address: Molecular and Analytical Development, Bristol-Myers Squibb, 311 Pennington Rocky Hill Road, Pennington, New Jersey 08534, United States

[#]Present Address: Chevron Phillips Chemical, 1862 Kingwood Drive, Kingwood, TX 77339, United States

[⊥]Present Address: Chemical Engineering & Applied Chemistry, University of Toronto, 200 College Street, Toronto, Ontario M5S 3E5, Canada

Corresponding Author*:

Telephone: 206-685-4964. E-mail:spiro@chem.washington.edu

ACKNOWLEDGMENT

This work was supported by the National Science Foundation: award numbers CHE-1410353 and CHE-1807222 to TGS, CHE-1410688 and CHE-1807158 to BMT, and an NSF Postdoctoral Research Fellowship in Biology Award ID: DBI-1202859 to CAR. Sincere thanks are expressed to Dr. Andy Kim for help with the DLS measurements, performed at the Department of

Chemical Engineering, University of Washington, and to Dr. George Blouin for help with Raman measurements.

REFERENCES

1. Morgan, J. J., Manganese in natural waters and Earth's crust: Its availability to organisms. In *Metal ions in biological systems: Manganese and its role in biological processes*, Sigel, A.; Sigel, H., Eds. Marcel Dekker: New York, 2000; Vol. 37, pp 1–34.

2. Post, J. E., Manganese oxide minerals: Crystal structures and economic and environmental significance. *Proc. Natl. Acad. Sci. U.S.A.* **1999,** *96*, 3447–3454.

3. Myers, C. R.; Nealson, K. H., Bacterial manganese reduction and growth with manganese oxide as the sole electron-acceptor. *Science* **1988,** *240*, 1319–1321.

4. Lovley, D. R., Dissimilatory Fe(III) and Mn(IV) reduction. *Microbiol. Rev.* **1991,** *55*, 259–287.

5. Lin, H.; Szeinbaum, N. H.; DiChristina, T. J.; Taillefert, M., Microbial Mn(IV) reduction requires an initial one-electron reductive solubilization step. *Geochim. Cosmochim. Acta* **2012,** *99*, 179–192.

6. Fischer, T. B.; Heaney, P. J.; Jang, J.-H.; Ross, D. E.; Brantley, S. L.; Post, J. E.; Tien, M., Continuous time-resolved X-ray diffraction of the biocatalyzed reduction of Mn oxide. *Am. Mineral.* **2008,** *93*, 1929−1932.

7. Johnson, J. E.; Savalia, P.; Davis, R.; Kocar, B. D.; Webb, S. M.; Nealson, K. H.; Fischer, W. W., Real-time manganese phase dynamics during biological and abiotic manganese oxide reduction. *Environ. Sci. Technol.* **2016,** *50*, 4248−4258.

8. Jackson, D. D., The precipitation of iron, manganese, and aluminium by bacterial action. *J. Soc. Chem. Ind.* **1901,** *21*, 681–684.

9. Hastings, D.; Emerson, S., Oxidation of manganese by spores of a marine *Bacillus*: kinetic and thermodynamic considerations. *Geochim. Cosmochim. Acta* **1986,** *50*, 1819–1824.

10. Nealson, K. H.; Tebo, B. M.; Rosson, R. A., Occurrence and mechanisms of microbial oxidation of manganese. *Adv. Appl. Microbiol.* **1988,** *33*, 279–318.

11. Emerson, D., Microbial oxidation of Fe(II) and Mn(II) at circumneutral pH. In *Environmental Microbe-Metal Interactions*, Lovley, D. R., Ed. American Society for Microbiology: Washington, DC, 2000.

12. Brouwers, G.-J.; Vijgenboom, E.; Corstjens, P. L. A. M.; de Vrind, J. P. M.; de Vrind-de Jong, E. W., Bacterial Mn^{2+} oxidizing systems and multicopper oxidases: an overview of mechanisms and functions. *Geomicrobiol. J.* **2000,** *17*, 1–24.

13. Tebo, B. M.; Bargar, J. R.; Clement, B.; Dick, G.; Murray, K. J.; Parker, D.; Verity, R.; Webb, S. M., Biogenic manganese oxides: Properties and mechanisms of formation. *Annu. Rev. Earth Planet. Sci.* **2004,** *32*, 287–328.

14. Tebo, B. M.; Johnson, H. A.; McCarthy, J. K.; Templeton, A. S., Geomicrobiology of manganese(II) oxidation. *Trends Microbiol.* **2005,** *13*, 421–428.

15. Miyata, N.; Tani, Y.; Sakata, M.; Iwahori, K., Microbial manganese oxide formation and interaction with toxic metal ions. *J. Biosci. Bioengin.* **2007,** *104*, 1–8.

16. Santelli, C. M.; Pfister, D.; Lazarus, D.; Sun, L.; Burgos, W. D.; Hansel, C. M., Diverse fungal and bacterial communities promote Mn(II)-oxidation and remediation of coal mine drainage in passive treatment systems *Appl. Environ. Microbiol.* **2010,** *76*, 4871–4875.

521 17. Santelli, C. M.; Webb, S. M.; Dohnalkova, A. C.; Hansel, C. M., Diversity of Mn oxides
522 produced by Mn(II)-oxidizing fungi. *Geochim. Cosmochim. Acta* **2011,** *75*, 2762–2776.
523 18. Hansel, C. M.; Zeiner, C. A.; Santelli, C. M.; Webb, S. M., Mn(II) oxidation by an
524 *Ascomycete* fungus is linked to superoxide production during asexual reproduction. *Proc. Natl.*
525 *Acad. Sci. U.S.A.* **2012,** *109*, 12621–12625.
526 19. Learman, D. R.; Voelker, B. M.; Vazquez-Rodriguez, A. I.; Hansel, C. M., Formation of
527 manganese oxides by bacterially generated superoxide. *Nat. Geosci.* **2011,** *4*, 95–98.
528 20. Learman, D. R.; Wankel, S. D.; Webb, S. M.; Martinez, N.; Madden, A. S.; Hansel, C. M.,
529 Coupled biotic-abiotic Mn(II) oxidation pathway mediates the formation and structural evolution
530 of biogenic Mn oxides. *Geochim. Cosmochim. Acta* **2011,** *75*, 6048–6063.
531 21. Learman, D. R.; Voelker, B. M.; Madden, A. S.; Hansel, C. M., Constraints on superoxide
532 mediated formation of manganese oxides. *Front. Microbiol.* **2013,** *4*, 262.
533 22. Andeer, P. F.; Learman, D. R.; McIlvin, M.; Dunn, J. A.; Hansel, C. M., Extracellular haem
534 peroxidases mediate Mn(II) oxidation in a marine *Roseobacter* bacterium via superoxide
535 production. *Environ. Microbiol.* **2015,** *17*, 3925–3936.
536 23. Anderson, C. R.; Johnson, H. A.; Caputo, N.; Davis, R. E.; Torpey, J. W.; Tebo, B. M.,
537 Mn(II) oxidation is catalyzed by heme peroxidases in "*Aurantimonas manganoxydans*" strain
538 SI85-9A1 and *Erythrobacter* sp. strain SD-21. *Appl. Environ. Microbiol.* **2009,** *75*, 4130–4138.
539 24. Geszvain, K.; Smesrud, L.; Tebo, B. M., Identification of a third Mn(II) oxidase enzyme in
540 *Pseudomonas putida* GB-1. *Appl. Environ. Microbiol.* **2016,** *82*, 3774–3782.
541 25. Corstjens, P. L. A. M.; de Vrind, J. P. M.; Goosen, T.; de Vrind-de Jong, E. W.,
542 Identification and molecular analysis of the *Leptothrix discophora* SS-1 mofA gene a gene
543 putatively encoding a manganese-oxidizing protein with copper domains. *Geomicrobiol. J.* **1997,**
544 *14*, 91–108.
545 26. Geszvain, K.; McCarthy, J. K.; Tebo, B. M., Elimination of manganese(II,III) oxidation in
546 *Pseudomonas putida* GB-1 by a double knockout of two putative multicopper oxidase genes.
547 *Appl. Environ. Microbiol.* **2013,** *79*, 357–366.
548 27. Brouwers, G.-J.; de Vrind, J. P. M.; Corstjens, P. L. A. M.; Cornelis, P.; Baysse, C.; de
549 Vrind-de Jong, E. W., CumA, a gene encoding a multicopper oxidase, is involved in Mn^{2+}-
550 oxidation in *Pseudomonas putida* GB-1. *Appl. Environ. Microbiol.* **1999,** *65*, 1762–1768.
551 28. van Waasbergen, L. G.; Hildebrand, M.; Tebo, B. M., Identification and characterization of a
552 gene cluster involved in manganese oxidation by spores of the marine *Bacillus* sp. strain SG-1. *J.*
553 *Bacteriology* **1996,** *178*, 3517–3530.
554 29. Dick, G. J.; Podell, S.; Johnson, H. A.; Rivera-Espinoza, Y.; Bernier-Latmani, R.; McCarthy,
555 J. K.; Torpey, J. W.; Clement, B. G.; Gaasterland, T.; Tebo, B. M., Genomic insights into Mn(II)
556 oxidation by the marine alphaproteobacterium *Aurantimonas* sp. strain SI85-9A1. *Appl. Environ.*
557 *Microbiol.* **2008,** *74*, 2646–2658.
558 30. Dick, G. J.; Torpey, J. W.; Beveridge, T. J.; Tebo, B. M., Direct identification of a bacterial
559 manganese(II) oxidase, the multicopper oxidase MnxG, from spores of several different marine
560 *Bacillus* species. *Appl. Environ. Microbiol.* **2008,** *74*, 1527–1534.
561 31. Francis, C. A.; Casciotti, K. L.; Tebo, B. M., Localization of Mn(II)-oxidizing activity and
562 the putative multicopper oxidase, MnxG, to the exosporium of the marine *Bacillus* sp. strain SG-
563 1. *Arch. Microbiol.* **2002,** *178*, 450–456.
564 32. Larsen, E. I.; Sly, L. I.; McEwan, A. G., Manganese(II) adsorption and oxidation by whole
565 cells and a membrane fraction of *Pedomicrobium* sp. ACM 3067. *Arch. Microbiol.* **1999,** *171*,
566 257–264.

33. Ridge, J. P.; Lin, M.; Larsen, E. I.; Fegan, M.; McEwan, A. G.; Sly, L. I., A multicopper oxidase is essential for manganese oxidation and laccase-like activity in *Pedomicrobium* sp. ACM 3067. *Environ. Microbiol.* **2007,** *9*, 944–953.
34. Butterfield, C. N.; Soldatova, A. V.; Lee, S.-W.; Spiro, T. G.; Tebo, B. M., Mn(II,III) oxidation and MnO_2 mineralization by an expressed bacterial multicopper oxidase. *Proc. Natl. Acad. Sci. U.S.A.* **2013,** *110*, 11731–11735.
35. Romano, C. A.; Zhou, M.; Song, Y.; Wysocki, V. H.; Dohnalkova, A. C.; Kovarik, L.; Paša-Tolić, L.; Tebo, B. M., Biogenic manganese oxide nanoparticle formation by a multimeric multicopper oxidase Mnx. *Nat. Commun.* **2017,** *8*, 746.
36. Soldatova, A. V.; Tao, L.; Romano, C.; Stich, T. A.; Casey, W. H.; Britt, R. D.; Tebo, B. M.; Spiro, T. G., Mn(II) oxidation by the multicopper oxidase complex Mnx: A binuclear activation mechanism. *J. Am. Chem. Soc.* **2017,** *139*, 11369−11380.
37. Soldatova, A. V.; Romano, C.; Tao, L.; Stich, T. A.; Casey, W. H.; Britt, R. D.; Tebo, B. M.; Spiro, T. G., Mn(II) oxidation by the multicopper oxidase complex Mnx: A coordinated two-stage MnII/MnIII and MnIII/MnIV mechanism. *J. Am. Chem. Soc.* **2017,** *139*, 11381−11391.
38. Bargar, J. R.; Tebo, B. M.; Villinski, J. E., In situ characterization of Mn(II) oxidation by spores of the marine *Bacillus* sp. strain SG-1. *Geochim. Cosmochim. Acta* **2000,** *64*, 2775−2778.
39. Villalobos, M.; Toner, B.; Bargar, J.; Sposito, G., Characterization of the manganese oxide produced by Pseudomonas putida strain MnB1. *Geochim. Cosmochim. Acta* **2003,** *67*, 2649–2662.
40. Miyata, N.; Tani, Y.; Iwahori, K.; Soma, M., Enzymatic formation of manganese oxides by an *Acremonium*-like hyphomycete fungus, strain KR21-2. *FEMS Microbiol. Ecol.* **2004,** *47*, 101–109.
41. Bargar, J. R.; Tebo, B. M.; Bergmann, U.; Webb, S. M.; Glatzel, P.; Chiu, V. Q.; Villalobos, M., Biotic and abiotic products of Mn(II) oxidation by spores of the marine *Bacillus* sp. strain SG-1. *Am. Mineral.* **2005,** *90*, 143–154.
42. Webb, S. M.; Tebo, B. M.; Bargar, J. R., Structural characterization of biogenic manganese oxides produced in sea water by the marine *Bacillus* sp. strain SG-1. *Am. Mineral.* **2005,** *90*, 1342–1357.
43. Zhu, M.; Ginder-Vogel, M.; Parikh, S. J.; Feng, X.-H.; Sparks, D. L., Cation effects on the layer structure of biogenic Mn-oxides. *Environ. Sci. Technol.* **2010,** *44*, 4465–4471.
44. Saratovsky, I.; Wightman, P. G.; Pasten, P. A.; Gaillard, J.-F.; Poeppelmeier, K. R., Manganese oxides: Parallels between abiotic and biotic structures. *J. Am. Chem. Soc.* **2006,** *128*, 11188–11198.
45. Webb, S. M.; Fuller, C. C.; Tebo, B. M.; Bargar, J. R., Determination of uranyl incorporation into biogenic manganese oxides using x-ray absorption spectroscopy and scattering. *Environ. Sci. Technol.* **2006,** *40*, 771–777.
46. Feng, X. H.; Zhu, M.; Ginder-Vogel, M.; Ni, C.; Parikh, S. J.; Sparks, D. L., Formation of nano-crystalline todorokite from biogenic Mn oxides. *Geochim. Cosmochim. Acta* **2010,** *74*, 3232–3245.
47. Tang, Y.; Webb, S. M.; Estes, E. R.; Hansel, C. M., Chromium(iii) oxidation by biogenic manganese oxides with varying structural ripening. *Environ. Sci. Process. Impact* **2014,** *16*, 2127−2136.
48. Spiro, T. G.; Bargar, J. R.; Sposito, G.; Tebo, B. M., Bacteriogenic manganese oxides. *Acc. Chem. Res.* **2010,** *43*, 2–9.

49. Remucal, C. K.; Ginder-Vogel, M., A critical review of the reactivity of manganese oxides with organic contaminants. *Environ. Sci. Process. Impacts* **2014,** *16*, 1247–1266.
50. Liu, W.; Sutton, N. B.; Rijnaarts, H. H. M.; Langenhoff, A. A. M., Pharmaceutical removal from water with iron- or manganese-based technologies: A review. *Crit. Rev. Environ. Sci. Technol.* **2016,** *46*, 1584–1621.
51. Sunda, W. G.; Kieber, D. J., Oxidation of humic substances by manganese oxides yields low-molecular-weight organic substrates. *Nature* **1994,** *367*, 62–64.
52. Robinson, D. M.; Go, Y. B.; Mui, M.; Gardner, G.; Zhang, Z.; Mastrogiovanni, D.; Garfunkel, E.; Li, J.; Greenblatt, M.; Dismukes, G. C., Photochemical water oxidation by crystalline polymorphs of manganese oxides: structural requirements for catalysis. *J. Am. Chem. Soc.* **2013,** *135*, 3494−3501.
53. Wiechen, M.; Spiccia, L., Manganese oxides as efficient water oxidation catalysts. *ChemCatChem* **2014,** *6*, 439–441.
54. Hocking, R. K.; Brimblecombe, R.; Chang, L.-Y.; Singh, A.; Cheah, M. H.; Glover, C.; Casey, W. H.; Spiccia, L., Water-oxidation catalysis by manganese in a geochemical-like cycle. *Nat. Chem.* **2011,** *3*, 461–466.
55. Huynh, M.; Shi, C.; Billinge, S. J. L.; Nocera, D. G., Nature of activated manganese oxide for oxygen evolution. *J. Am. Chem. Soc.* **2015,** *137*, 14887−14904.
56. Frey, C. E.; Wiechen, M.; Kurz, P., Water-oxidation catalysis by synthetic manganese oxides – systematic variations of the calcium birnessite theme. *Dalton Trans.* **2014,** *43*, 4370–4379.
57. Meng, Y.; Song, W.; Huang, H.; Ren, Z.; Chen, S.-Y.; Suib, S. L., Structure−property relationship of bifunctional MnO_2 nanostructures: highly efficient, ultra-stable electrochemical water oxidation and oxygen reduction reaction catalysts identified in alkaline media. *J. Am. Chem. Soc.* **2014,** *136*, 11452–11464.
58. McKendry, I. G.; Thenuwara, A. C.; Shumlas, S. L.; Peng, H.; Aulin, Y. V.; Rao Chinnam, P.; Borguet, E.; Strongin, D. R.; Zdilla, M. J., Systematic doping of cobalt into layered manganese oxide sheets substantially enhances water oxidation catalysis. *Inorg. Chem.* **2018,** *57*, 557−564.
59. Lucht, K. P.; Mendoza-Cortes, J. L., Birnessite: A layered manganese oxide to capture sunlight for water-splitting catalysis. *J. Phys. Chem. C* **2015,** *119*, 2838−22846.
60. Le Goff, P.; Baffier, N.; Bach, S.; Pereira-Ramos, J.-P., Structural and electrochemical properties of layered manganese dioxides in relation to their synthesis: Classical and sol-gel routes. *J. Mater. Chem.* **1994,** *4*, 875–881.
61. Devaraj, S.; Munichandraiah, N., Effect of crystallographic structure of MnO_2 on its electrochemical capacitance properties. *J. Phys. Chem. C* **2008,** *112*, 4406–4417.
62. Sassin, M. B.; Chervin, C. N.; Rolison, D. R.; Long, J. W., Redox deposition of nanoscale metal oxides on carbon for next-generation electrochemical capacitors. *Acc. Chem. Res.* **2013,** *46*, 1062−1074.
63. Wei, W.; Cui, X.; Chen, W.; Ivey, D. G., Manganese oxide-based materials as electrochemical supercapacitor electrodes. *Chem. Soc. Rev.* **2011,** *40*, 1697−1721.
64. Gao, P.; Metz, P.; Hey, T.; Gong, Y.; Liu, D.; Edwards, D. D.; Howe, J. Y.; Huang, R.; Misture, S. T., The critical role of point defects in improving the specific capacitance of d-MnO_2 nanosheets. *Nat. Commun.* **2017,** *8*, 14559.
65. El-Kady, M. F.; Ihns, M.; Li, M.; Hwang, J. Y.; Mousavi, M. F.; Chaney, L.; Lech, A. T.; Kaner, R. B., Engineering three-dimensional hybrid supercapacitors and microsupercapacitors

for high-performance integrated energy storage. *Proc. Natl. Acad. Sci. U.S.A.* **2015,** *112*, 4233−4238.
66. Khojasteh, M.; Haghighat, S.; Dawlaty, J. M.; Kresin, V. V., Controlled deposition of size-selected MnO nanoparticle thin films for water splitting applications: reduction of onset potential with particle size. *Nanotechnology* **2018,** *29,* 215603.
67. Villalobos, M.; Bargar, J.; Sposito, G., Mechanisms of Pb(II) sorption on a biogenic manganese oxide. *Environ. Sci. Technol.* **2005,** *39*, 569–576.
68. Osterloh, F. E., Inorganic nanostructures for photoelectrochemical and photocatalytic water splitting. *Chem. Soc. Rev.* **2013,** *42*, 2294–2320.
69. Marafatto, F. F.; Lanson, B.; Peña, J., Crystal growth and aggregation in suspensions of δ-MnO_2 nanoparticles: implications for surface reactivity. *Environ. Sci. Nano* **2018,** *5*, 497–508.
70. Wigginton, N. S.; Haus, K. L.; Hochella Jr, M. F., Aquatic environmental nanoparticles. *J. Environ. Monit.* **2007,** *9*, 1306–1316.
71. McKenzie, R. M., The synthesis of birnessite, cryptomelane, and some other oxides and hydroxides of manganese. *Mineral. Mag.* **1971,** *38*, 493–502.
72. Perez-Benito, J.; Brillas, E.; Pouplana, R., Identification of a soluble form of colloidal manganese(IV). *Inorg. Chem.* **1989,** *28*, 390–392.
73. Perez-Benito, J. F., Reduction of colloidal manganese dioxide by manganese(II). *J. Colloid Interface Sci.* **2002,** *248*, 130–135.
74. Butterfield, C. N.; Tebo, B. M., Substrate specificity and copper loading of the manganese-oxidizing multicopper oxidase Mnx from *Bacillus* sp. PL-12. *Metallomics* **2017,** *9*, 183–191.
75. Malvern Instruments. (2007). Sample dispersion and refractive index guide. Mastersizer 2000 reference manual. Worcestershire, U.K.
76. Gillespie, J. B.; Lindberg, J. D., Ultraviolet and visible imaginary refractive index of strongly absorbing atmospheric particulate matter. *Appl. Opt.* **1992,** *31*, 2112–2115.
77. Lume-Pereira, C.; Baral, S.; Henglein, A.; Janata, E., Chemistry of colloidal manganese dioxide. 1. Mechanism of reduction by an organic radical (a radiation chemical study). *J. Phys. Chem.* **1985,** *89*, 5772–5718.
78. Sakai, N.; Ebina, Y.; Takada, K.; Sasaki, T., Photocurrent generation from semiconducting manganese oxide nanosheets in response to visible light. *J. Phys. Chem. B* **2005,** *109*, 9651–9655.
79. Huangfu, X.; Jiang, J.; Ma, J.; Liu, Y.; Yang, J., Aggregation kinetics of manganese dioxide colloids in aqueous solution: Influence of humic substances and biomacromolecules. *Environ. Sci. Technol.* **2013,** *47*, 10285−10292.
80. Siebecker, M.; Madison, A. S.; Luther III, G. W., Reduction kinetics of polymeric (soluble) manganese (IV) oxide (MnO_2) by ferrous iron (Fe^{2+}). *Aquat. Geochem.* **2015,** *21*, 143–158.
81. Kwon, K. D.; Refson, K.; Sposito, G., On the role of Mn(IV) vacancies in the photoreductive dissolution of hexagonal birnessite. *Geochim. Cosmochim. Acta* **2009,** *73*, 4142–4150.
82. Sherman, D. M., Electronic structures of iron(III) and manganese(IV) (hydr)oxide minerals: Thermodynamics of photochemical reductive dissolution in aquatic environments. *Geochim. Cosmochim. Acta* **2005,** *69*, 3249–3255.
83. Murray, J. W., The surface chemistry of hydrous manganese dioxide. *J. Colloid Interface Sci.* **1974,** *46*, 357–371.
84. Perez-Benito, J.; Arias, C.; Amat, E., A kinetic study of the reduction of colloidal manganese dioxide by oxalic acid. *J. Colloid Interface Sci.* **1996,** *177*, 288–297.

85. Yao, W.; Millero, F. J., Adsorption of phosphate on manganese dioxide in seawater. *Environ. Sci. Technol.* **1996,** *30*, 536–541.
86. Wang, Q.; Liao, X.; Xu, W.; Ren, Y.; Livi, K. J.; Zhu, M., Synthesis of birnessite in the presence of phosphate, silicate, or sulfate. *Inorg. Chem.* **2016,** *55*, 10248−10258.
87. Grassian, V. H., When size really matters: Size-dependent properties and surface chemistry of metal and metal oxide nanoparticles in gas and liquid phase environments. *J. Phys. Chem. C* **2008,** *112*, 18303–18313.
88. Burda, C.; Chen, X.; Narayanan, R.; El-Sayed, M. A., Chemistry and properties of nanocrystals of different shapes. *Chem. Rev.* **2005,** *105*, 1025−1102.
89. Sun, J.; Goldys, E. M., Linear absorption and molar extinction coefficients in direct semiconductor quantum dots. *J. Phys. Chem. C* **2008,** *112*, 9261–9266.
90. Liu, X.; Atwater, M.; Wang, J.; Huo, Q., Extinction coefficient of gold nanoparticles with different sizes and different capping ligands. *Colloids Surf. B* **2007,** *58*, 3–7.
91. Yu, W. W.; Qu, L.; Guo, W.; Peng, X., Experimental determination of the extinction coefficient of CdTe, CdSe, and CdS nanocrystals. *Chem. Mater.* **2003,** *15*, 2854–2860.
92. Roduner, E., Size matters: why nanomaterials are different. *Chem. Soc. Rev.* **2006,** *35*, 583–592.
93. Brock, S. L.; Sanabria, M.; Suib, S. L.; Urban, V.; Thiyagarajan, P.; Potter, D. I., Particle size control and self-assembly processes in novel colloids of nanocrystalline manganese oxide. *J. Phys. Chem. B* **1999,** *103*, 7416–7428.
94. Gao, T.; Glerup, M.; Krumeich, F.; Nesper, R.; Fjellvåg, H.; Norby, P., Microstructures and spectroscopic properties of cryptomelane-type manganese dioxide nanofibers. *J. Phys. Chem. C* **2008,** *112*, 13134–13140.
95. Jung, H.; Chadha, T. S.; Min, Y.; Biswas, P.; Jun, Y.-S., Photochemically-assisted synthesis of birnessite nanosheets and their structural alteration in the presence of pyrophosphate. *ACS Sustain. Chem. Eng.* **2017,** *5*, 10624−10632.
96. Tauc, J.; Grigorovici, R.; Vancu, A., Optical properties and electronic structure of amorphous germanium. *Phys. Stat. Sol.* **1966,** *15*, 627–637.
97. Kwon, K. D.; Refson, K.; Sposito, G., Defect-induced photoconductivity in layered manganese oxides: A Density Functional Theory study. *Phys. Rev. Lett.* **2008,** *100*, 146601.
98. Viezbicke, B. D.; Patel, S.; Davis, B. E.; Birnie III, D. P., Evaluation of the Tauc method for optical absorption edge determination: ZnO thin films as a model system. *Phys. Status Solidi B* **2015,** *252*, 1700–1710.
99. Link, S.; El-Sayed, M. A., Size and temperature dependence of the plasmon absorption of colloidal gold nanoparticles. *J. Phys. Chem. B* **1999,** *103*, 4212–4217.
100. Mullaugh, K. M.; Luther III, G. W., Spectroscopic determination of the size of cadmium sulfide nanoparticles formed under environmentally relevant conditions. *J. Environ. Monit.* **2010,** *12*, 890–897.
101. Borgohain, K.; Murase, N.; Mahamunia, S., Synthesis and properties of Cu_2O quantum particles. *J. Appl. Phys.* **2002,** *92*, 1292–1297.
102. Pesika, N. S.; Stebe, K. J.; Searson, P. C., Relationship between absorbance spectra and particle size distributions for quantum-sized nanocrystals. *J. Phys. Chem. B* **2003,** *107*, 10412–10415.
103. Zhang, H.; Bayne, M.; Fernando, S.; Legg, B.; Zhu, M.; Penn, R. L.; Banfield, J. F., Size-dependent bandgap of nanogoethite. *J. Phys. Chem. C* **2011,** *115*, 17704–17710.

104. Brus, L. E., Electron–electron and electron-hole interactions in small semiconductor crystallites: The size dependence of the lowest excited electronic state. *J. Chem. Phys.* **1984,** *80*, 4403–4409.
105. Pinaud, B. A.; Chen, Z.; Abram, D. N.; Jaramillo, T. F., Thin films of sodium birnessite-type MnO_2: optical properties, electronic band structure, and solar photoelectrochemistry. *J. Phys. Chem. C* **2011,** *115*, 11830–11838.
106. Zhou, F.; McDonnell-Worth, C.; Li, H.; Li, J.; Spiccia, L.; Macfarlane, D. R., Enhanced photo-electrochemical water oxidation on MnO_x in buffered organic/inorganic electrolytes. *J. Mater. Chem. A* **2015,** *3*, 16642–16652.
107. Lany, S., Semiconducting transition metal oxides. *J. Phys. Condens. Matter* **2015,** *27*, 283203.
108. Tvrdy, K.; Frantsuzov, P. A.; Kamat, P. V., Photoinduced electron transfer from semiconductor quantum dots to metal oxide nanoparticles. *Proc. Natl. Acad. Sci. U.S.A.* **2011,** *108*, 29–34.
109. The 0.5 mM PP point was not plotted because the DLS-measured size of the particles fell off the trend. We inferred that the DLS technique, which measures hydrodynamic diameter of a particle that includes salvation shell and adsorbates that move along with the particle, overestimated the nanoparticle size because of higher association of strongly adsorbing PP at 0.5 mM PP concentration. Nevertheless, the band gap energy of 0.5 mM PP colloid, which correlates with the intrinsic MnO_2 properties, follows the expected trend (Table S1).
110. Buciuman, F.; Patcas, F.; Craciun, R.; Zahn, D. R. T., Vibrational spectroscopy of bulk and supported manganese oxides. *Phys. Chem. Chem. Phys.* **1999,** *1*, 185–190.
111. Julien, C. M.; Massot, M.; Poinsignon, C., Lattice vibrations of manganese oxides - Part 1. Periodic structures. *Spectrochim. Acta A* **2004,** *60*, 689–700.
112. Kim, H.-S.; Stair, P. C., Bacterially produced manganese oxide and todorokite: UV Raman spectroscopic comparison. *J. Phys. Chem. B* **2004,** *108*, 17019–17026.
113. Gao, T.; Fjellvag, H.; Norby, P., Structural and morphological evolution of β-MnO_2 nanorods during hydrothermal synthesis. *Nanotechnology* **2009,** *20*, 055610.
114. Julien, C.; Massot, M.; Baddour-Hadjean, R.; Franger, S.; Bach, S.; Pereira-Ramos, J. P., Raman spectra of birnessite manganese dioxides. *Solid State Ion.* **2003,** *159* 345–356.
115. Chen, D.; Ding, D.; Li, X.; Waller, G. H.; Xiong, X.; El-Sayed, M. A.; Liu, M., Probing the charge storage mechanism of a pseudocapacitive MnO_2 electrode using *in operando* Raman spectroscopy. *Chem. Mater.* **2015,** *27*, 6608−6619.
116. Morgan Chan, Z.; Kitchaev, D. A.; Nelson Weker, J.; Schnedermann, C.; Lim, K.; Ceder, G.; Tumas, W.; Toney, M. F.; Nocera, D. G., Electrochemical trapping of metastable Mn^{3+} ions for activation of MnO_2 oxygen evolution catalysts. *Proc. Natl. Acad. Sci. U.S.A.* **2018,** *115*, E5261–E5268.
117. Momma, K.; Izumi, F., VESTA 3 for three-dimensional visualization of crystal, volumetric and morphology data. *J. Appl. Crystallogr.* **2011,** *44*, 1272–1276.
118. Gaillot, A.-C.; Flot, D.; Drits, V. A.; Manceau, A.; Burghammer, M.; Lanson, B., Structure of synthetic K-rich birnessite obtained by high-temperature decomposition of $KMnO_4$. I. Two-layer polytype from 800 °C experiment. *Chem. Mater.* **2003,** *15*, 4666–4678.
119. Zhu, M.; Farrow, C. L.; Post, J. E.; Livi, K. J. T.; Billinge, S. J. L.; Ginder-Vogel, M.; Sparks, D. L., Structural study of biotic and abiotic poorly-crystalline manganese oxides using atomic pair distribution function analysis. *Geochim. Cosmochim. Acta* **2012,** *81*, 39–55.

120. Ling, F. T.; Heaney, P. J.; Post, J. E.; Gao, X., Transformations from triclinic to hexagonal birnessite at circumneutral pH induced through pH control by common biological buffers. *Chem. Geol.* **2015,** *416*, 1–10.
121. Lotya, M.; Rakovich, A.; Donegan, J. F.; Coleman, J. N., Measuring the lateral size of liquid-exfoliated nanosheets with dynamic light scattering. *Nanotechnology* **2013,** *24*, 265703.
122. Elzinga, E. J., Reductive transformation of birnessite by aqueous Mn(II). *Environ. Sci. Technol.* **2011,** *45*, 6366–6372.
123. Lefkowitz, J. P.; Rouff, A. A.; Elzinga, E. J., Influence of pH on the reductive transformation of birnessite by aqueous Mn(II). *Environ. Sci. Technol.* **2013,** *47*, 10364−10371.
124. Klewicki, J. K.; Morgan, J. J., Kinetic behavior of Mn(III) complexes of pyrophosphate, EDTA, and citrate. *Environ. Sci. Technol.* **1998,** *32*, 2916–2922.
125. Fendorf, S. E.; Sparks, D. L.; Franz, J. A.; Camaioni, D. M., Electron Paramagnetic Resonance stopped-flow kinetic study of manganese (II) sorption-desorption on birnessite. *Soil Sci. Soc. Am. J.* **1993,** *57*, 57–62.
126. Simanova, A. A.; Peña, J., Time-resolved investigation of cobalt oxidation by Mn(III)-rich δ-MnO_2 using quick X-ray absorption spectroscopy. *Environ. Sci. Technol.* **2015,** *49*, 10867−10876.
127. Peña, J.; Bargar, J. R.; Sposito, G., Copper sorption by the edge surfaces of synthetic birnessite nanoparticles. *Chem. Geol.* **2015,** *396*, 196–207.
128. Wang, Y.; Benkaddour, S.; Marafatto, F. F.; Peña, J., Diffusion- and pH-dependent reactivity of layer-type MnO_2: Reactions at particle edges versus vacancy sites. *Environ. Sci. Technol.* **2018,** *52*, 3476−3485.
129. Simanova, A. A.; Kwon, K. D.; Bone, S. E.; Bargar, J. R.; Refson, K.; Sposito, G.; Peña, J., Probing the sorption reactivity of the edge surfaces in birnessite nanoparticles using nickel(II). *Geochim. Cosmochim. Acta* **2015,** *164*, 191–204.
130. Stone, A. T.; Morgan, J. J., Reduction and dissolution of manganese(III) and manganese(IV) oxides by organics. 1. Reaction with hydroquinone. *Environ. Sci. Technol.* **1984,** *18*, 450–456.
131. Zhao, H.; Zhu, M.; Li, W.; Elzinga, E. J.; Villalobos, M.; Liu, F.; Zhang, J.; Feng, X.; Sparks, D. L., Redox reactions between Mn(II) and hexagonal birnessite change its layer symmetry. *Environ. Sci. Technol.* **2016,** *50*, 1750–1758.
132. Wang, Q.; Yang, P.; Zhu, M., Structural transformation of birnessite by fulvic acid under anoxic conditions. *Environ. Sci. Technol.* **2018,** *52*, 1844−1853.
133. Villinski, J. E.; O'Day, P. A.; Corley, T. L.; Conklin, M. H., *In situ* spectroscopic and solution analyses of the reductive dissolution of MnO_2 by Fe(II). *Environ. Sci. Technol.* **2001,** *35*, 1157–1163.
134. Lefkowitz, J. P.; Elzinga, E. J., Impacts of aqueous Mn(II) on the sorption of Zn(II) by hexagonal birnessite. *Environ. Sci. Technol.* **2015,** *49*, 4886−4893.
135. Lafferty, B. J.; Ginder-Vogel, M.; Zhu, M.; Livi, K. J. T.; Sparks, D. L., Arsenite oxidation by a poorly crystalline manganese-oxide. 2. Results from X-ray absorption spectroscopy and X-ray diffraction. *Environ. Sci. Technol.* **2010,** *44*, 8467–8472.
136. Feng, X.; Wang, P.; Shi, Z.; Kwon, K. D.; Zhao, H.; Yin, H.; Lin, Z.; Zhu, M.; Liang, X.; Liu, F.; Sparks, D. L., A quantitative model for the coupled kinetics of arsenic adsorption/desorption and oxidation on manganese oxides. *Environ. Sci. Technol. Lett.* **2018,** *5*, 175−180.

137. Miyata, N.; Maruo, K.; Tani, Y.; Tsuno, H.; Seyama, H.; Soma, M.; Iwahori, K., Production of biogenic manganese oxides by anamorhic ascomycete fungi isolated from streambed pebbles. *Geomicrobiol. J.* **2006,** *23*, 63–73.
138. Özkar, S.; Finke, R. G., Palladium(0) nanoparticle formation, stabilization, and mechanistic studies: $Pd(acac)_2$ as a preferred precursor, $[Bu_4N]_2HPO_4$ stabilizer, plus the stoichiometry, kinetics, and minimal, four-step mechanism of the palladium nanoparticle formation and subsequent agglomeration reactions. *Langmuir* **2016,** *32*, 3699−3716.
139. Peng, X.; Wickham, J.; Alivisatos, A. P., Kinetics of II-VI and III-V colloidal semiconductor nanocrystal growth: "Focusing" of size distributions. *J. Am. Chem. Soc.* **1998,** *120*, 5343–5344.
140. Jiang, F.; Muscat, A. J., Ligand-controlled growth of ZnSe quantum dots in water during Ostwald ripening. *Langmuir* **2012,** *28*, 12931−12940.
141. Clark, M. D., Growth laws for surfactant-coated nanocrystals: Ostwald ripening and size focusing. *J. Nanopart. Res.* **2014,** *16*, 2264–2264.
142. Wang, F.; Richards, V. N.; Shields, S. P.; Buhro, W. E., Kinetics and mechanisms of aggregative nanocrystal growth. *Chem. Mater.* **2014,** *26*, 5−21.
143. Bunker, B. C.; Casey, W. H., *The aqueous chemistry of oxides*. Oxford University Press: New York, 2016.
144. Huang, F.; Zhang, H.; Banfield, J. F., Two-stage crystal-growth kinetics observed during hydrothermal coarsening of nanocrystalline ZnS. *Nano Lett.* **2003,** *3*, 373–378.
145. Gilbert, B.; Zhang, H.; Huang, F.; Finnegan, M. P.; Waychunas, G. A.; Banfield, J. F., Special phase transformation and crystal growth pathways observed in nanoparticles. *Geochem. Trans.* **2003,** *4*, 20–27.
146. Zhang, J.; Huang, F.; Lin, Z., Progress of nanocrystalline growth kinetics based on oriented attachment. *Nanoscale* **2010,** *2*, 18–34.
147. Liang, X.; Zhao, Z.; Zhu, M.; Liu, F.; Wang, L.; Yin, H. Q., G.; Cao, F.; Liu, X.; Feng, X., Self-assembly of birnessite nanoflowers by staged three-dimensional oriented attachment. *Environ. Sci. Nano* **2017,** *4*, 1656–1669.
148. Hopenhayn, C., Arsenic in drinking water: impact on human health. *Elements* **2006,** *2*, 103–107.
149. Yogarajah, N.; Tsai, S. S. H., Detection of trace arsenic in drinking water: challenges and opportunities for microfluidics. *Environ. Sci. Water Res. Technol.* **2015,** *1*, 426–447.
150. Mohanty, D., Conventional as well as emerging arsenic removal technologies—a critical review. *Water Air Soil Pollut.* **2017,** *228*, 381.
151. Schacht, L.; Ginder-Vogel, M., Arsenite depletion by manganese oxides: A case study on the limitations of observed first order rate constants. *Soil Syst.* **2018,** *2*, 39.
152. Lafferty, B. J.; Ginder-Vogel, M.; Sparks, D. L., Arsenite oxidation by a poorly crystalline manganese-oxide 1. Stirred-flow experiments. *Environ. Sci. Technol.* **2010,** *44*, 8460–8466.
153. Manning, B. A.; Fendorf, S. E.; Bostick, B.; Suarez, D. L., Arsenic(III) oxidation and arsenic(V) adsorption reactions on synthetic birnessite. *Environ. Sci. Technol.* **2002,** *36*, 976−981.
154. Villalobos, M.; Escobar-Quiroz, I. N.; Salazar-Camacho, C., The influence of particle size and structure on the sorption and oxidation behavior of birnessite: I. Adsorption of As(V) and oxidation of As(III). *Geochim. Cosmochim. Acta* **2014,** *125*, 564–581.

881 155. Oscarson, D. W.; Huang, P. M.; Defosse, C.; Herbillon, A., Oxidative power of Mn(IV) and
882 Fe(III) oxides with respect to As(III) in terrestrial and aquatic environments. *Nature* **1981,** *291*,
883 50–51.
884 156. Coddington, K., A review of arsenicals in biology. *Toxicol. Environ. Chem.* **1986,** *11*, 281–
885 290.
886 157. Shen, S.; Li, X.-F.; Cullen, W. R.; Weinfeld, M.; Le, X. C., Arsenic binding to proteins.
887 *Chem. Rev.* **2013,** *113*, 7769−7792.
888 158. Wang, Z.; Lee, S.-W.; Kapoor, P.; Tebo, B. M.; Giammar, D. E., Uraninite oxidation and
889 dissolution induced by manganese oxide: A redox reaction between two insoluble minerals.
890 *Geochim. Cosmochim. Acta* **2013,** *100*, 24–40.
891 159. Webb, S. M.; Dick, G. J.; Bargar, J. R.; Tebo, B. M., Evidence for the presence of Mn(III)
892 intermediates in the bacterial oxidation of Mn(II). *Proc. Natl. Acad. Sci. U.S.A.* **2005,** *102*, 5558–
893 5563.
894
895

896 **TABLE OF CONTENTS FIGURE**

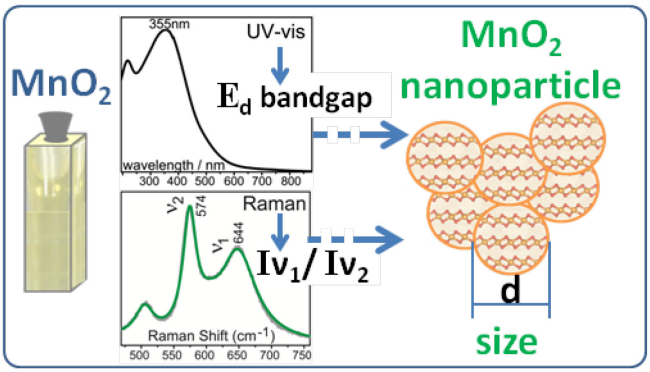

897